

Tethered-particle model: The calculation of free energies for hard-sphere systems

Cite as: *J. Chem. Phys.* **155**, 064504 (2021); doi: [10.1063/5.0058892](https://doi.org/10.1063/5.0058892)

Submitted: 3 June 2021 • Accepted: 27 July 2021 •

Published Online: 11 August 2021



View Online



Export Citation



CrossMark

Craig Moir,^{1,2,a)}  Leo Lue,³  and Marcus N. Bannerman¹ 

AFFILIATIONS

¹School of Engineering, University of Aberdeen, Aberdeen AB24 3UE, United Kingdom

²Curtin Institute for Computation, Curtin University, P.O. Box U1987, Perth, Western Australia 6845, Australia

³Department of Chemical and Process Engineering, University of Strathclyde, James Weir Building, 75 Montrose Street, Glasgow G1 1XJ, United Kingdom

^{a)} Author to whom correspondence should be addressed: craig.moir3@abdn.ac.uk

ABSTRACT

Two methods for computing the entropy of hard-sphere systems using a spherical tether model are explored, which allow the efficient use of event-driven molecular-dynamics simulations. An intuitive derivation is given, which relates the rate of particle collisions, either between two particles or between a particle and its respective tether, to an associated hypersurface area, which bounds the system's accessible configurational phase space. Integrating the particle-particle collision rates with respect to the sphere diameter (or, equivalently, density) or the particle-tether collision rates with respect to the tether length then directly determines the volume of accessible phase space and, therefore, the system entropy. The approach is general and can be used for any system composed of particles interacting with discrete potentials in fluid, solid, or glassy states. The entropies calculated for the liquid and crystalline hard-sphere states using these methods are found to agree closely with the current best estimates in the literature, demonstrating the accuracy of the approach.

Published under an exclusive license by AIP Publishing. <https://doi.org/10.1063/5.0058892>

I. INTRODUCTION

The equilibrium thermodynamic properties of a material, including its phase behavior, are dictated by the dependence of its free energy on the state variables. For fluids, the free energy relative to the ideal-gas state can be accurately determined by a straightforward thermodynamic integration with density. Crystalline states, however, are typically separated from fluid states (and, consequently, the ideal gas) by a first-order transition. Interfacial effects will dominate in any direct crystal-solid co-existence simulation; thus, other indirect methods need to be employed to reliably calculate the free energy.

There have been a number of attempts to modify model fluids to construct a continuous thermodynamic path between an ideal state and the crystalline state. Hoover and Ree originally introduced the single occupancy (SO) cell model¹ to demonstrate the existence of a first-order melting transition for hard-sphere systems and quantitatively determined the fluid and solid coexistence densities. In the SO model, space is partitioned into cells based on Voronoi polyhedra created from the sites of the crystal lattice under investigation,

for example, the face-centered cubic (FCC) lattice. The center of each particle is then constrained to remain in its respective cell. This model lowers the entropy of the fluid state by preventing free movement, and this softens, but does not eliminate, the first order freezing transition. Regardless, thermodynamic integration can be carried out over this small transition to connect the crystalline and ideal gas states, and this was successfully used to settle a long debate over the most stable structure for mono-sized spheres.^{2,3} In crystalline states, the SO cell model and unmodified hard-sphere system are assumed to be equal, as the particles themselves confine each other to the centers of the Voronoi polyhedra, thus preventing interactions with the SO cell boundaries. This method was used to quantitatively demonstrate that the FCC lattice is more stable than the HCP lattice for hard-sphere systems.

A variation of the SO model was later proposed by Speedy,⁴ where the particles are instead restricted to remain within a set distance from their respective lattice sites rather than within Voronoi polyhedra (i.e., they are tethered to a lattice). This tethered particle model (TPM) used spherical square-well potential as the tether potential, which allows more efficient simulation of cell

collisions and somewhat simplifies the theoretical analysis. This is the foundation of the approach adopted and extended in this work.

This spherical tether approach has been generalized to arbitrarily shaped particles and implemented using an event-driven molecular dynamics (MD) algorithm,⁵ although the derivation is limited to near-jammed conditions (e.g., solid states that are dynamically arrested). This was successfully used to accurately calculate the free energy of different crystal phases, as well as glassy states, of hard-sphere systems. Many other approaches use a tethering potential to tie particles to specific positions (e.g., a lattice) to determine the free energy of the untethered crystal/jammed system. In the Einstein crystal approach for obtaining the free energy of crystalline systems,^{6,7} molecules are tethered to the sites of a perfect lattice using a harmonic potential. The stiffness of the potential can be continuously adjusted, and this can be used to relate the system back to a perfect Einstein crystal, where the molecules do not interact significantly with each other and which has an exactly known free energy. This continuous transformation between the system and the perfect Einstein crystal can be used to compute the free energy of the system.

Other more elaborate methods that involve the use of tethers have been developed in order to more efficiently calculate the free energy, such as the self-referential methods reported by Sweatman and co-workers,^{8–10} the Schilling–Schmid algorithm,¹¹ and the interface pinning method.¹² These are nicely compared and reviewed by Sweatman.¹³ More generally, tether models can be considered as confining the motion of the system to a particular region in phase space. Typically, only the positional degrees of freedom are tethered; however, restricted velocity dynamics have also proven useful^{14,15} and may be considered a form of tethering in phase space. The consideration of the effect of the tether in configurational phase space is a crucial concept to the derivations presented here.

For simplicity, this work focuses on hard-sphere systems although it readily generalizes to any particle system that interacts through discrete potentials. Hard-sphere systems play an important role in the understanding of the behavior of fluids and solids. They capture the excluded volume interactions between molecules, which often dominate the structure of fluids.¹⁶ Consequently, hard spheres have often been used as a starting point for the development of perturbation theories for more complex models. The tether model of Speedy⁴ is revisited here, and a novel approach for calculating free energy in any state, including fluids, glasses, or crystals, is

derived. As a demonstration of the efficiency of the approach, new high accuracy free energy calculations for the hard-sphere crystal are performed.

The remainder of this paper is organized as follows: In Sec. II, the tether model of Speedy is revisited. The collision statistics and thermodynamics of this model are described, including the ideal tether model, where the spheres do not interact with each other, and its relationship with the standard ideal gas model is established. It is demonstrated that the tether model can provide a continuous path between the fluid and solid phases, which avoids crossing a first order phase transition for certain ranges of the tether length. In Sec. III, the collision rates of tethered systems, with both other spheres and the tethering potential that keeps the spheres within their cells, are related to the geometry of phase space. In particular, these collision rates are directly related to the areas of surfaces that bound the region of phase space that is accessible by the system. These relations are used to develop a method to compute the free energy of hard-sphere systems via an integration with the tether length. In Sec. IV, these methods are used to determine the free energy of hard-sphere systems at various densities within the fluid and solid phases. These calculations are all found to agree well with those previously given in the literature. Finally, the key results of this paper are summarized in Sec. V along with a discussion of directions for future work.

II. THE TETHERED PARTICLE MODEL

This work considers a system of hard-sphere particles tethered to a lattice using a square-well potential that is equal to zero within a spherical region around the tether point and infinitely large outside this region. This forces the center of each particle to remain within a tether “cell” and is precisely the model first introduced by Speedy.⁴ A schematic representation of the system is presented in Fig. 1. The tether forces particles to be within a distance r_T of their respective tether point, and so, each particle center can explore at most a volume V_T . This allows the definition of a tether packing fraction $\phi_T = \rho V_T$ (where ρ is the particle number density), which may take values greater than one if tether volumes overlap, as depicted in Fig. 1.

For particles tethered to points in a regular lattice, there is a density $\rho_{T,0}$ below which the tether cells become separated by more than a particle diameter σ , and the particles can no longer interact with each other. This density can be easily calculated from the maximum packing fraction of the lattice. For example, for

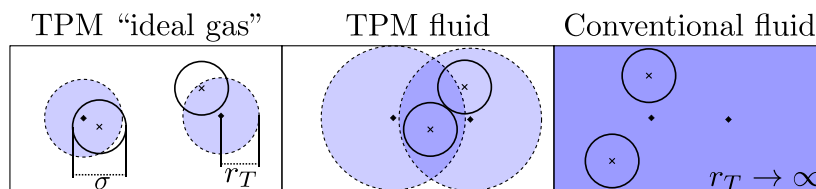


FIG. 1. Schematic diagram of a two-dimensional tethered particle system in three different states: the “ideal” TPM (left) has particles tethered such that no particle–particle interactions can occur. The TPM fluid (middle) allows interactions, and the conventional fluid (right) is simply the limit of infinite tether length. Black circles represent particles with diameter σ , and black crosses represent the position of the particle centers. Dashed shaded circles represent the confining tether cells with radius r_T whose centers are indicated with black diamonds.

particles tethered to a face-centered cubic (FCC) lattice, the density is given by

$$\rho_{T,0}^{\text{FCC}} \sigma^3 = \max\left(0, \left[2^{1/6} - \left(\frac{6\phi_T}{\pi}\right)^{1/3}\right]^3\right). \quad (1)$$

The max function prevents negative densities when tether cells overlap, i.e., beyond the close-packed density $\phi_T \geq \sqrt{2}\pi/6$. From this expression, a minimum tether radius $r_{T,0}$ at which interactions can occur can also be defined. For an FCC lattice, it is given by

$$r_{T,0}^{\text{FCC}}/\sigma = \max\left(0, \left[2^{5/2}\rho\sigma^3\right]^{-1/3} - 1/2\right). \quad (2)$$

For $\rho < \rho_{T,0}$ (or, equivalently, $r_T < r_{T,0}$), there are only tether collisions and no particle–particle collisions. The system is in an “ideal” state, where the particles are independent of each other and the pressure p is given by the ideal gas law [i.e., $\beta p = \rho$, where $\beta = 1/(k_B T)$ and k_B is the Boltzmann constant]. It should be noted that the system is not ergodic in this limit as collisional paths within a spherical domain preserve the angle of incidence between the boundary and the particle. Previous work⁴ has avoided this issue by ensuring $r_T > r_{T,0}$; however, in this work, it is preferred to thermalize the system with a stochastic Andersen thermostat to provide rapid equilibration near the ideal state. The thermostat event mean free time is controlled to be $\sim 5\%$ of the total event count, which was chosen as it is a small additional computational cost of processing the thermostat events while providing rapid thermal equilibration. Each thermostat event randomly selects a single particle and reassigns its velocity from a Gaussian distribution. This allows the collection of precise points for all tether lengths, which, however, increases the drift in the center-of-mass of the system, which is discussed later.

The “ideal” TPM differs from the standard ideal gas for N particles in a volume V , as each particle can only explore a restricted volume V_T , and consequently, the particles are distinguishable. The difference between the specific entropy of the “ideal” tethered particle model $s_T^{(\text{ideal})}$ and a conventional ideal gas $s^{(\text{ig})}$ at the same temperature and density is then given as follows:

$$s_T^{(\text{ideal})}(\rho) - s^{(\text{ig})}(\rho) = \frac{k_B}{N} \ln \frac{\Omega_T^{(\text{ideal})}}{\Omega^{(\text{ig})}} = k_B \ln \left(\frac{\phi_T (N!)^{1/N}}{N} \right), \quad (3)$$

where $\Omega_T^{(\text{ideal})}$ and $\Omega^{(\text{ig})}$ are the microcanonical configurational partition functions (i.e., volume of configurational phase space accessible by the system) for the “ideal” TPM and the conventional ideal gas, respectively, and given by

$$\Omega^{(\text{ig})}(N, V) = \frac{V^N}{N!} \Omega_T^{(\text{ideal})}(N, V) = V_T^N. \quad (4)$$

The factor of $N!$ is absent for the TPM system because the particles are assigned to specific cells, making them distinguishable.

It is important to note that, for hard-sphere systems, there is only kinetic energy and there is no interaction energy; consequently, in the absence of an external field, the internal energy of hard-sphere systems has no configurational contribution and behaves identically to that of an ideal gas. In this case, the residual Helmholtz free energy F^{res} (i.e., deviation from an ideal gas with the same temperature, volume, and number of particles) is directly related to the residual entropy as $F^{\text{res}} = -TS^{\text{res}}$. The residual entropy is the focus of

this work, but it is interchangeable with the residual Helmholtz free energy.

The presence of the tether potential restricts the volume of phase space available to a system, and so, the entropy of the tethered system is always equal to or lower than that of the untethered system. The influence of the tether on the properties of the system is related to the frequency of the tether collisions. When $r_T < r_{T,0}$, the portion of phase space that can be explored by the system is fully dictated by the tether, and the system properties will be identical to those of the ideal tether particle model. As the tether length increases so that $r_T > r_{T,0}$ (or, equivalently, the density increases such that $\rho > \rho_{T,0}$), particle–particle interactions can take place. For moderate values of the density, tether collisions still occur, and the tether still acts to confine the system to a subset of its phase space; however, particle–particle overlaps now further restrict the system to a smaller region. This is referred to here as the tether “fluid” state. The tether potential decreases the entropy and, therefore, the stability of the fluid state. This reduction in stability can be controlled precisely by adjusting the tether length. Through proper choice of the tether length, the fluid state can be made less stable than the crystalline state, which is weakly affected by the presence of the tether, provided that the crystal prevents the diffusion of the particles. This might present an interesting opportunity to construct a continuous thermodynamic path between the ideal tether state and the crystalline state. The effect of tethering on the fluid–solid transition is explored in Sec. II A.

A. Fluid–solid transition in the tethered particle model

To illustrate the influence of the tether potential, calculations are performed for the systems of N hard spheres at constant absolute temperature T with diameter σ and mass m using DynamO, an open-source event-driven molecular dynamics (MD) simulation package.¹⁷ The key dimensionless parameters of the system are the reduced density $\rho\sigma^3$ and the reduced tether length r_T/σ .

The variation of the compressibility factor $Z = \beta p/\rho$ [where p is the pressure, $\beta = 1/(k_B T)$, and k_B is the Boltzmann constant] of the TPM with density is shown in Fig. 2 for different values of ϕ_T in comparison to the conventional hard-sphere system (i.e., with no tethering) and that of an ideal gas (where $Z = 1$). Simulations are not run below the minimum interaction density $\rho_{T,0}$ corresponding to each value of ϕ_T , as the compressibility factor is exactly equal to the ideal value (i.e., $Z = 1$) below this density. At moderate densities where $\rho > \rho_{T,0}$, the smaller tether volumes restrict the motion of the particles and thus reduce the particle–particle collision rate that is directly proportional to the system pressure. At densities above the crystal transition, all systems converge to the standard hard sphere crystal system, highlighting their equivalence in this limit.

For the untethered hard-sphere system, there is a first order transition from a fluid phase to a solid phase; the coexistence region is bracketed by the vertical dashed lines in Fig. 2. As expected, the simulations display a metastable fluid branch due to their finite size and duration; however, as ϕ_T decreases, the system appears to approach an extension of the crystalline branch with no indication of a first-order transition appearing for $\phi_T \approx 0.5$ and lower. This is confirmed by examining the numerical derivative of the pressure with density, which remains positive for $\phi_T \leq 0.5$ (see the inset of Fig. 2).

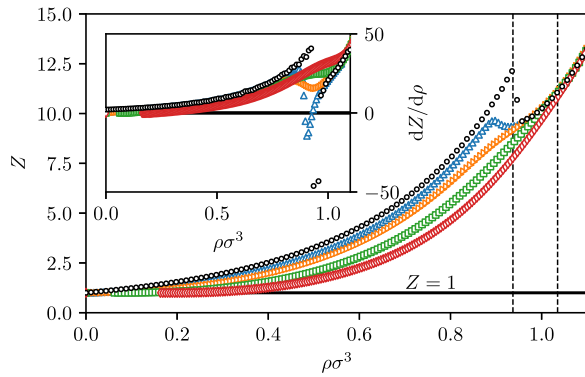


FIG. 2. The compressibility factor Z and its numerical derivative (inset) as a function of reduced density $\rho\sigma^3$ for hard-sphere TPM systems with $\phi_T = 0.1$ (red), $\phi_T = 0.2$ (green), $\phi_T = 0.5$ (orange), and $\phi_T = 1$ (blue). Data are shown for simulations containing $N = 2916$ spheres and are only run above $\rho > \rho_{T,0}$. Black circles represent conventional (untethered) hard-sphere simulations. The horizontal solid black line indicates ideal compressibility. Vertical dashed black lines highlight the untethered hard-sphere fluid–solid transition zone (freezing density, $\rho\sigma^3 \approx 0.937$; melting density, $\rho\sigma^3 \approx 1.035$). The standard deviation in pressure measurements is smaller than the symbol size.

Thus, for sufficiently small values of ϕ_T , there seems to be a continuous thermodynamic path between the high-density hard-sphere solid and the low density “ideal” tether model limit. This thermodynamic path can be easily understood in terms of a phase diagram for the tether model system and is depicted by the vertical dashed line labeled path 1 in Fig. 3. Thermodynamic integration along this path can be used to establish the entropy (and thus the free energy) of the crystalline state with respect to the ideal tether model, as given in Eq. (3).

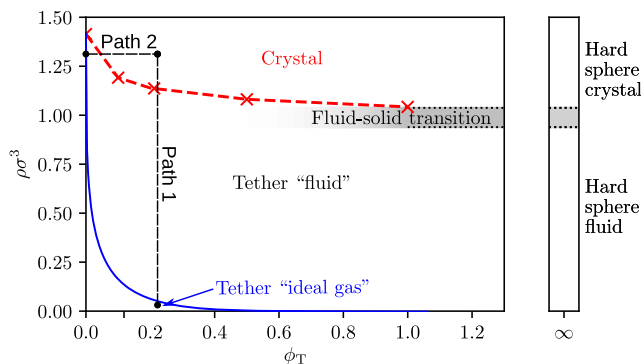


FIG. 3. An illustration of the reduced density $\rho\sigma^3$ and tether packing fractions ϕ_T at which the tethered hard-sphere system enters various “phases.” The crosses (red) indicate the upper density where an $N = 2916$ system run for 2×10^9 events had more than 100 tether events. The dashed line (red) is added as a guide to the eye to indicate that the systems above this density have crystallized on the tether lattice and particles cannot interact with their tether anymore. The point at $\phi_T = 0$ is exact and equal to the FCC close packing density $\rho\sigma^3 = \sqrt{2}$. The lower solid curve (blue) indicates that when the tether length prevents inter-particle interactions, it denotes the “ideal” tether state. The gray area is a guide to the eye and indicates where first-order transitions are observed numerically.

The red dashed line in Fig. 3 denotes a rough boundary above which tether events are so rare (in this case less than a fraction 10^{-7} of total events) that the system closely resembles the untethered hard sphere crystal; thus, the free energies of the tethered and untethered hard sphere crystals are assumed equal in this limit. The exact boundary of the ideal tether state is shown as a solid blue curve in Fig. 3, and it is immediately apparent that the ideal and crystalline states can be continuously connected using thermodynamic integration along a second path using the tether length as the variable (see path 2 in Fig. 3); however, it is not immediately apparent what the relevant thermodynamic force and work terms are in this case. Section III discusses this further, but first, the practicalities of implementing the standard thermodynamic integration approach along path 1 are outlined.

B. Thermodynamic integration

The entropy of a fluid hard-sphere system at any density can be obtained via thermodynamic integration with reference to the ideal gas state,

$$s^{\text{res}}(\rho) \equiv s(\rho) - s^{(\text{ig})}(\rho) = -k_B \int_0^\rho \frac{d\rho'}{\rho'} [Z(\rho') - 1], \quad (5)$$

where s^{res} is the residual entropy. This integration is also applicable to path 1 of Fig. 3 in the tether model for all densities as it is continuous and avoids the first-order transition. The tether model can then be related back to the untethered ideal gas by accounting for the difference in the entropy of the ideal states [see Eq. (3)],

$$\begin{aligned} s_T^{\text{res}}(\rho) &\equiv s_T(\rho) - s^{(\text{ig})}(\rho) \\ &= -k_B \int_{\rho_{T,0}}^\rho \frac{d\rho'}{\rho'} [Z_T(\rho') - 1] + k_B \ln \left((N!)^{1/N} \frac{\phi_T}{N} \right). \end{aligned} \quad (6)$$

The thermodynamic integration is chosen to begin at the density $\rho_{T,0}$ where particles begin to interact [i.e., Eq. (1)], as below this density, the integrand is zero. The only approximation required to determine the crystal state free energy of the untethered system is to assume the equivalence to the tethered system at sufficiently high densities: that is, for hard spheres that are limited to the FCC crystal,

$$s(\rho) = \lim_{\rho\sigma^3 \rightarrow \sqrt{2}} s_T(\rho). \quad (7)$$

This assumption is true in the FCC crystal, which prevents diffusion if care is taken to also prevent the center-of-mass drifting during simulation. Tether collisions do not preserve momentum, and so, Speedy⁴ modified his tether dynamics to rebalance the system momentum on tether impacts. This approach is not done here due to its computational cost; instead, this effect is explored while examining the system size dependence of the results.

III. PHASE SPACE GEOMETRY

In this section, the collision rates in a tethered hard-sphere system are related to the geometry of its phase space. The configurational phase space of a hard-sphere system is schematically depicted in Fig. 4(a). The space is constructed by collecting all

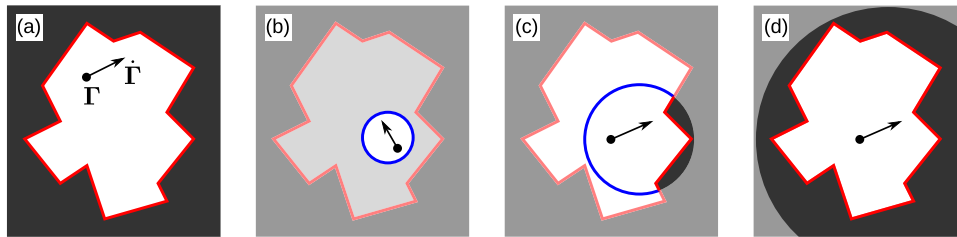


FIG. 4. A schematic depiction of configurational phase space for (a) a hard-sphere system, (b) a tightly tethered hard-sphere system, and (c) and (d) loosely tethered hard-sphere systems. The point illustrates a state of a system at a particular time ($\vec{\Gamma}$), and the arrow indicates its trajectory through phase space $\dot{\vec{\Gamma}}$. The dark areas are regions of phase space that are disallowed due to sphere–sphere overlaps, while the white areas correspond to the phase space volume accessible to the system. Regions are faded where the tether also prevents the system from entering them. The surfaces that bound the accessible region due to the tether potential are highlighted in blue, while the surfaces corresponding to particle–particle contact are highlighted in red. The tethered and untethered systems are exactly equivalent if the accessible regions are the same [i.e., (a) \equiv (d)]. This requires the system to be confined to a particular region of phase space by the interactions (i.e., a crystal without diffusion) and that the tether is sufficiently long for it to fall outside the accessible phase space [i.e., (d)].

the positions of the N hard spheres into a single vector $\vec{\Gamma} \equiv (\mathbf{r}_1, \mathbf{r}_2, \dots, \mathbf{r}_N)$, where \mathbf{r}_i is the position of sphere i in the system. This vector then traces out a trajectory over time within the configurational phase space with a velocity, $\dot{\vec{\Gamma}} \equiv (\mathbf{v}_1, \mathbf{v}_2, \dots, \mathbf{v}_N)$, where \mathbf{v}_i is the velocity of sphere i in the system. Excluded volume interactions between the spheres will prohibit the system from entering regions in phase space where spheres overlap (depicted by the dark area in Fig. 4), thus confining the trajectory of the system to within an “accessible” region [white area in Fig. 4(a)]. The hypervolume Ω of this accessible phase space is directly related to the entropy of the system by the Boltzmann–Planck equation $S = k_B \ln \Omega$. The boundary between the allowed and disallowed regions of phase space (depicted by the red line in Fig. 4) corresponds to two spheres being in contact with each other aside from some measure-zero higher-order contacts, and this boundary has an associated hypersurface area Σ .

A hard-sphere system evolving through time traces a straight line through phase space as there are no forces between collisions. Collisions between spheres correspond to the trajectory reflecting from a point on the phase space boundary corresponding to where the colliding pair of spheres is in contact; the trajectory will then reflect from the boundary and continue to travel in a straight line until it encounters another boundary in phase space. The process is then repeated.

When a square-well tether potential is applied, the accessible region of phase space becomes an intersection of the N tether volumes and the accessible volume of the untethered system. An illustration of two systems with different tether lengths is given in Figs. 4(b) and 4(c). The tether restricts the motion of the system, and the system trajectory can now reflect off the tether boundary [see the blue line in Figs. 4(b) and 4(c)]. For short enough tether lengths, the system can only interact with the tether [see Fig. 4(b)]; however, at longer tether lengths, portions of the sphere–sphere collision boundary will intrude into the accessible region [see Fig. 4(c)]. If the exposed hypersurface area of the tether potential [see the blue line in Fig. 4(c)] can be measured, it can be numerically “extruded” by varying the tether length, and thus, the accessible volume can be measured. Sections III A–III C detail the specifics of this approach and how hypersurface areas in phase space might be linked to collision rates.

A. Collision rates and hypersurface areas in phase space

If the system is ergodic, the hypersurface area of the various boundaries that confine the system to a particular region of phase space is directly related to the rate at which the system collides with the respective boundary. In this picture, standard kinetic theory arguments give an expression for the average collision rate $\dot{\mathcal{N}}$ that the system makes with a section of the phase space boundary of the area Σ as follows:

$$\dot{\mathcal{N}} = \rho_\Omega \Sigma \langle \dot{\vec{\Gamma}} \cdot \hat{\mathbf{n}}_\Sigma \rangle, \quad (8)$$

where $\hat{\mathbf{n}}_\Sigma$ is a unit vector that is normal to the surface pointing outward from the accessible phase space volume and ρ_Ω is the number density of systems in the phase space. As only one system is considered to be inside phase space here, $\rho_\Omega = 1/\Omega$. This leads to the first main result of this section as follows:

$$\frac{\Sigma}{\Omega} = \frac{\dot{\mathcal{N}}}{\langle \dot{\vec{\Gamma}} \cdot \hat{\mathbf{n}}_\Sigma \rangle}. \quad (9)$$

The ratio of the hypersurface area to the accessible phase space volume is directly related to the collision rate of the system with this hypersurface, divided by the mean velocity of its approach to the hypersurface. Therefore, the various collision rates give an indication of the relative exposed hypersurface areas corresponding to each type of event (i.e., collision between spheres or collision between a sphere and its tether potential). In Secs. III B and III C, these different collisions are considered in more detail.

B. Particle–particle collisions

For hard-sphere systems, points in phase space where two particles overlap are not accessible (the black region in Fig. 4). The region of phase space the system is allowed to explore is bounded by surfaces that correspond to configurations where various pairs of particles are in contact (the red line in Fig. 4). If the diameter σ of the hard spheres increases by $d\sigma$, the excluded region of phase space will become larger, and the allowed region of phase space will become smaller (i.e., $d\Omega < 0$). This corresponds to the bounding surfaces being displaced normally by a distance $d\sigma$ inward toward the

accessible volume of phase space. The corresponding decrease in the accessible volume is quantitatively given by

$$d\Omega = -\Sigma d\sigma. \quad (10)$$

The negative sign appears because an increase in the particle diameter decreases the accessible phase space volume. Using Eq. (9), we can relate this to the particle–particle collision rate $\dot{\mathcal{N}}$,

$$d \ln \Omega = -\frac{\dot{\mathcal{N}}}{\langle \dot{\Gamma} \cdot \hat{\mathbf{n}}_{\Sigma} \rangle} d\sigma. \quad (11)$$

The projection of the velocity $\dot{\Gamma}$ of the system normal to the surface is simply the relative velocity of the colliding pair of spheres, which is distributed according to the following equation:

$$f_{\text{rel}}(\mathbf{v}) = (2\pi\beta\mu)e^{-\beta\mu v^2/2}, \quad (12)$$

where $\mu = m/2$ is the reduced mass of the colliding pair of spheres. As a result, the mean speed at which the system approaches a phase space boundary corresponding to a sphere–sphere collision is given by

$$\langle \dot{\Gamma} \cdot \hat{\mathbf{n}}_{\Sigma} \rangle = \langle \mathbf{v}_{jk} \cdot \hat{\mathbf{r}}_{jk} \rangle = (\pi\beta m)^{-1/2}, \quad (13)$$

where j and k are the indices of two colliding particles, $\mathbf{r}_{jk} = \mathbf{r}_j - \mathbf{r}_k$ is their relative position, and $\mathbf{v}_{jk} = \mathbf{v}_j - \mathbf{v}_k$ is their relative velocity.

For a fixed number of particles, a change in the particle diameter can be considered as a change in the density/volume of the system,

$$d\sigma = -\frac{\sigma}{DV} dV, \quad (14)$$

where D is the dimensionality (in this case, $D = 3$). Substituting this relation and Eq. (13) into Eq. (11) yields the following result:

$$\begin{aligned} d \ln \Omega &= \frac{d\Omega}{\Omega} = \frac{\Sigma}{\Omega} \frac{\sigma}{DV} dV, \\ \frac{\partial \ln \Omega}{\partial V} &= \beta p = \frac{\Sigma}{\Omega} \frac{\sigma}{DV}, \end{aligned} \quad (15)$$

where it should be noted that the derivative of the entropy is directly related to the pressure p of the system.

The above expression for the pressure accounts only for portions of phase space excluded by sphere overlaps. If the spheres in the system are confined to a particular volume in space, then there will be an additional term corresponding to the ideal gas contribution. If the portion of collisions of the system with some boundary is included, then the following equation is obtained:

$$\frac{\beta p}{\rho} = 1 + \frac{\sigma}{D} \frac{\Sigma}{N\Omega}. \quad (16)$$

It is interesting to note the similarity of this expression to that of Speedy,¹⁸

$$\frac{\beta p}{\rho} = 1 + \frac{\sigma}{2D} \frac{S_0}{V_0}, \quad (17)$$

where V_0 is the average volume available for the insertion of an additional sphere and S_0 is the average surface area of that volume, and the expression given by Hoover *et al.*¹⁹ is as follows:

$$\frac{\beta p}{\rho} = 1 + \frac{\sigma}{2D} \left\langle \frac{S_f}{V_f} \right\rangle, \quad (18)$$

where V_f is the volume available for the center of a given sphere to move when all other spheres are frozen in their positions and S_f is the surface area of that volume.

If the expression for the phase space area over volume in terms of the collision rate, given in Eq. (9), is substituted into Eq. (16), the pressure can be written as follows:

$$\frac{\beta p}{\rho} = 1 + \frac{\sigma}{DN} (\pi\beta m)^{1/2} \dot{\mathcal{N}}. \quad (19)$$

This is simply the standard collision rate expression for the system pressure for hard-sphere systems.^{20,21} While this result is not new, it validates the approach to be used for tether collisions, which can provide a direct measurement of free-energy changes.

C. Tether collisions

For a tethered system, the accessible phase space will be restricted not only by particle–particle overlaps but also by the tether. Increasing the length of the tether will potentially increase the volume of phase space accessible to the system. To determine the accessible volume Ω_T of phase space for the tethered model, the hypersurface area Σ_T associated with the tether interactions that are accessible by the system can be extruded by moving it slightly outward in a direction normal to the hypersurface (i.e., parallel to $\hat{\mathbf{n}}_{\Sigma_T}$). For the spherical tether potential used in this study, this extrusion is easily achieved by increasing the tether length by an infinitesimal distance dr_T ,

$$d\Omega_T = \Sigma_T dr_T. \quad (20)$$

This relation holds true as the tether potential hypersurface can only be reached by the system if it appears in the accessible phase space volume of the untethered model (see Fig. 4), which then becomes the accessible region of the tethered model upon extrusion. If phase space is not simply connected, then this extrusion may only measure the volume of phase space accessible to the initial ensemble, which allows interesting studies of dynamically arrested states, such as glasses.⁴

A change of variables directly relates the change in the accessible volume to the change in the entropy of the system,

$$k_B^{-1} ds_T = N^{-1} d \ln \Omega_T = \frac{\Sigma_T}{N\Omega_T} dr_T = \frac{\dot{\mathcal{N}}_T}{N\langle \dot{\Gamma} \cdot \hat{\mathbf{n}}_{\Sigma_T} \rangle} dr_T. \quad (21)$$

A straightforward integration yields the entropy change of a tethered system with a change in the tether length,

$$s_T(\rho, r_{T,2}) - s_T(\rho, r_{T,1}) = k_B \langle \dot{\Gamma} \cdot \hat{\mathbf{n}}_{\Sigma_T} \rangle^{-1} \int_{r_{T,1}}^{r_{T,2}} dr_T \frac{\dot{\mathcal{N}}_T}{N}. \quad (22)$$

The system is assumed to be at constant temperature so that the “velocity” $\dot{\Gamma}$ of the system through phase space is given by the Maxwell–Boltzmann distribution. This implies that the velocities of

each of the spheres are independent of each other and also given by the Maxwell–Boltzmann distribution,

$$f(\mathbf{v}) = (2\pi\beta m)^{-3/2} e^{-\beta m v^2/2}. \quad (23)$$

As each tether acts separately on a single particle, the surface of phase space associated with it is parallel to the degrees of freedom (dimensions) that correspond to the other particles. Therefore, during an intersection with a tether hypersurface, other particles do not contribute to $\dot{\Gamma} \cdot \hat{\mathbf{n}}_{\Sigma_T}$ and only the velocity of the confined particle is relevant. Additionally, only the component that is normal to the surface contributes, and thus, the average phase trajectory velocity into the tether boundary is given as follows:

$$\langle \dot{\Gamma} \cdot \hat{\mathbf{n}}_{\Sigma_T} \rangle = \langle \mathbf{v} \cdot \hat{\mathbf{n}} \rangle = (2\pi\beta m)^{-1/2}. \quad (24)$$

Combining this with Eq. (22) leads to the remarkably simple result that entropy changes with the tether length can be determined by simply monitoring the tether collision rate during a series of simulations at different tether lengths.

To relate the tethered system to the untethered system for the purpose of computing its entropy, two types of states are considered. The first are states like those in a crystalline phase, where the untethered system is confined to a phase space volume, which is relatively localized around the configuration of the tether points due to close packing of its constituent particles. In this case, a tethered system with a long tether should not undergo tether collisions as these will be precluded by particle–particle collisions. In fact, verifying that the tether events have reached zero is a test of this condition. At these conditions, the tethered system has exactly the same “absolute” entropy as the untethered system, exploring the same phase space volume [see Fig. 4(d)]. The entropy for systems in these types of states can be calculated by combining Eqs. (22) and (24) to yield

$$\begin{aligned} s^{\text{res}}(\rho) &= s(\rho) - s^{(\text{ig})}(\rho) \\ &= \lim_{r_T \rightarrow \infty} s_T(\rho, r_T) - s^{(\text{ig})}(\rho) \\ &= k_B (2\pi\beta m)^{1/2} \int_{r_{T,0}}^{\infty} dr_T \frac{\dot{N}_T}{N} + k_B \ln \left(\frac{(N!)^{1/N} \phi_{T,0}}{N} \right). \end{aligned} \quad (25)$$

The integration has been shifted to start at the onset of particle interactions for computational efficiency. Donev *et al.*⁵ used a closely related approach to compute the entropy, where the integral is performed in a single simulation where the tether length grows with time; however, their derivation is restricted to close to the jammed state and uses dynamic integration, whereas Eq. (25) is evaluated at equilibrium. The practical usefulness of Eq. (25) depends on the tether event rate approaching zero (i.e., $\dot{N}_T \rightarrow 0$) at some finite value of r_T so that the integral can be truncated; however, this is not the case for fluid systems that will always interact with the tether.

For systems in the fluid state, tether collisions will occur no matter how long the tether length because, given enough time, particles will eventually diffuse to the edge of their tether “cell.” The entropy of tether systems in the fluid state can be related to untethered systems by noting that the fraction of phase space excluded by particle overlaps is the same for the tethered and untethered models

in the limit of infinite tether length,

$$\frac{\Omega(N, V)}{\Omega^{(\text{ig})}(N, V)} = \lim_{r_T \rightarrow \infty} \frac{\Omega_T(N, V, r_{mT})}{\Omega_T^{(\text{ideal})}(N, V, r_T)}, \quad (26)$$

$$s(\rho) - s^{(\text{ig})}(\rho) = \lim_{r_T \rightarrow \infty} \left(s_T(\rho, r_T) - s_T^{(\text{ideal})}(\rho, r_T) \right). \quad (27)$$

Applying Eq. (22) twice for the tethered and ideal tethered systems gives the following identity:

$$s(\rho) - s^{(\text{ig})}(\rho) = k_B N^{-1} (2\pi\beta m)^{1/2} \int_{r_{T,0}}^{\infty} dr_T \left(\dot{N}_T - \dot{N}_T^{(\text{ideal})} \right), \quad (28)$$

where the lower bound of the integral can be $r_{T,0}$ as below this, the integrand is zero. The ideal rate of tether events $\dot{N}_T^{(\text{ideal})}$ can be obtained via straightforward kinetic arguments or by a derivative of the ideal tether entropy in Eq. (3) with the tether length,

$$(2\pi\beta m)^{1/2} \dot{N}_T^{(\text{ideal})} = \frac{DN}{r_T}. \quad (29)$$

Thus, Eq. (25) provides a convenient thermodynamic integration path for crystalline state points, while Eq. (28) provides a path for fluid state points.

Whether Eq. (25) or (28) is practically useful depends on how quickly the integrals converge. To explore this, simulation results for the tether collision rate are presented in Fig. 5 for a fluid system and a crystal system. Both integrals converge remarkably quickly, which is surprising for the fluid state but reflects the lack of long-range order in the system. The minimum tether rate for the liquid system indicates the onset of melting of the tether lattice, unlike in the solid system.

To verify the convergence behavior, the kernels of Eqs. (25) and (28) are plotted in the semi-log axis in Fig. 6. For the liquid

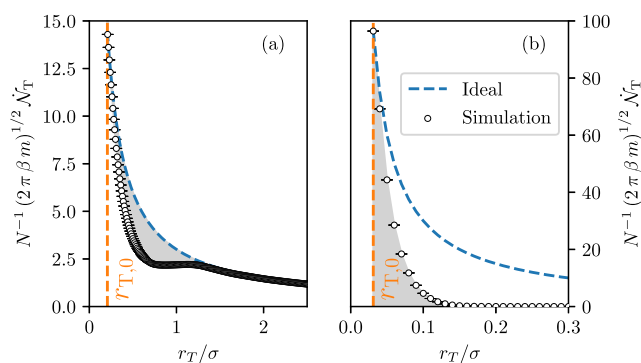


FIG. 5. The variation of the tether event rate \dot{N}_T as a function of the reduced tether length r_T/σ for an NVT ensemble hard-sphere system tethered to an FCC lattice with $N = 8788$ at a reduced density of (a) $\rho\sigma^3 = 0.5$ and (b) $\rho\sigma^3 = 1.2$. The (blue) dashed line represents the reduced ideal tether event rate of Eq. (29). In the left figure, the gray shaded area between the ideal event rate and the measured tether event rate shows the integral of Eq. (28) used to calculate the entropy of fluid systems. The shaded area below the measured cell event rate in the right figure shows the integral of Eq. (25) used when calculating the solid entropy. The vertical red dashed line shows the minimum cell radius r_T at which it is possible for particles to interact with each other as given by Eq. (2).

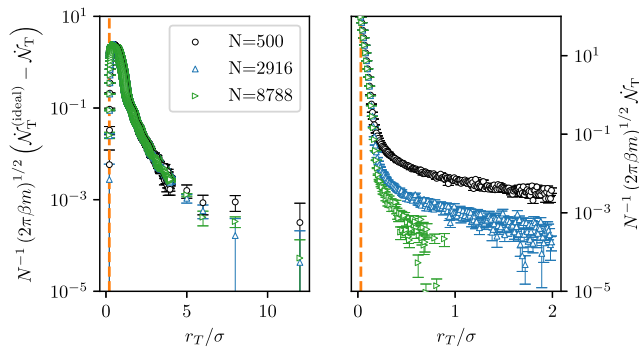


FIG. 6. The kernel of the integral of Eq. (28) at $\rho\sigma^3 = 0.5$ (left) and Eq. (25) at $\rho\sigma^3 = 1.18$ as a function of the tether length for an NVT hard-sphere system. A long decay is apparent in the fluid integral (left) and also appears in the solid system (right); however, it decreases with system size and even disappears for large enough systems, despite relatively high event counts for equilibration ($10^4 N$) and production ($10^5 N$) due to the slow center-of-mass diffusion dynamics.

state, a tail persists to long tether lengths. Rather than attempting to close this contribution by fitting an exponential tail, it is simply truncated at long tether lengths for simplicity as its contribution is small. The solid-state results demonstrate an interesting N^{-1} dependence in the magnitude of the tail. This effect can be explained by the drift of the simulation center-of-mass, causing interactions with the tether to appear at large tether lengths. At larger system sizes, the center-of-mass drift is lower due to the higher averaging of the thermal fluctuations, reducing the center-of-mass velocity. Ultimately, the larger system sizes are not run for long enough for the center-of-mass to drift within the interaction range of the tether, leading to the early truncation of the tail compared to smaller system sizes. As this effect is system size dependent, it will be removed later during the extrapolation to $N \rightarrow \infty$.

D. Summary

In this section, particle–particle and particle–tether event rates in hard-sphere systems are linked to the geometry of their accessible phase space. Particle–particle collision rates are shown to be directly related to the pressure, in agreement with previous work. Tether collision rates are found to provide a method to calculate the volume of accessible phase space (and thus also the system entropy). In Sec. IV, two techniques for calculating the system entropy are applied to the hard-sphere system to compute the phase diagram.

IV. CALCULATION OF THE ENTROPY

In this section, estimates for the entropy of hard-sphere systems are obtained using the two methods described in Secs. II and III. The first approach uses MD simulation runs at a single value of ϕ_T while different densities are sampled (i.e., path 1 from Fig. 3). The second approach uses simulation runs at a single density while a range of tether lengths are sampled (i.e., path 2 from Fig. 3). All simulations are initialized in an FCC lattice, and the tether cell for each particle is centered on the FCC lattice site for that particle. Simulations are run over a range of system sizes, $N \in \{500, 864, 1372, 2048, 2916, 8788\}$, to allow an analysis of the size dependence. Simulations are equilibrated for $10^4 N$ events and run for at least $10^5 N$ total events,

TABLE I. Calculated residual entropy s^{res}/k_B for different system sizes N and number densities $\rho\sigma^3$ using the constant tether cell volume fraction integration (path 1 of Fig. 3). The uncertainty in the last reported digit is given in parenthesis.

N	$\rho\sigma^3 = 1.06$	$\rho\sigma^3 = 1.13$	$\rho\sigma^3 = 1.18$	$\rho\sigma^3 = 1.21$
500	-6.088 7(2)	-6.865 0(2)	-7.519 9(2)	-7.972 6(2)
864	-6.096 6(1)	-6.872 5(1)	-7.527 0(1)	-7.979 8(1)
1372	-6.100 6(1)	-6.876 54(9)	-7.531 0(1)	-7.985 (5)
2048	-6.103 11(9)	-6.878 89(8)	-7.533 17(8)	-7.986 05(5)
2916	-6.104 66(9)	-6.880 34(7)	-7.534 66(7)	-7.987 53(4)
∞	-6.107 8(4)	-6.883 5(3)	-7.537 7(4)	-7.990 6(4)

sometimes as long as $10^6 N$ events, to collect statistics. This is performed over ten or more production runs and three complete restarts (new particle velocities on the FCC lattice), which allows the estimation of the unbiased standard error in the mean values reported. These error estimates are propagated through the calculations to yield uncertainty estimates on all results, including the integration and fitting operations.

A. Path 1: Density integration

For path 1, the integration of Eq. (6) is performed at 4 separate cell volume fractions $\phi_T = 0.1, 0.2, 0.5,$ and 1.0 . Simulations are performed at 200 separate densities spaced evenly from $\rho_{T,0}$ to final densities $\rho\sigma^3 = 1.21, 1.18, 1.13,$ and 1.06 , respectively. These densities are sufficiently high for cell events to drop to zero in these simulations (see Fig. 3 for an illustration of this boundary). The trapezoidal rule is used to evaluate the integral of Eq. (6), and the individual entropy values obtained using this method are shown in Table I.

A linear fit in N^{-1} is used to extrapolate to $N \rightarrow \infty$, and an example extrapolation is given in Fig. 7. The extrapolations are all strongly linear, leading to a high confidence in the final results, which will be validated against the results from path 2 and the literature.

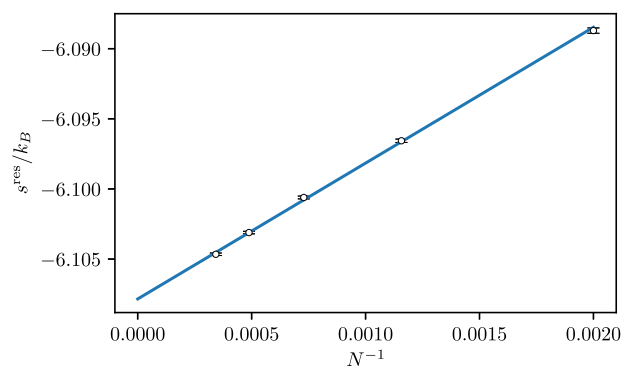


FIG. 7. Excess entropy as a function of particle number N calculated using simulations (points) with a tether cell volume fraction of $\phi_T = 0.5$ and a density of $\rho\sigma^3 = 1.06$. Error bars indicate the estimate of standard error in the integral values but are smaller than the symbols. The system sizes (right to left) are $N \in \{500, 864, 1372, 2048, 2916\}$, and the extrapolation (line) to give $N \rightarrow \infty$ yields an intercept of $-6.1078(4)$.

TABLE II. Calculated residual entropy s^{res}/k_B for different system sizes N and number densities $\rho\sigma^3$ using the varying tether radius integration (path 2). The uncertainty in the last reported digit is given in parenthesis.

N	$\rho\sigma^3 = 0.5$	$\rho\sigma^3 = 0.9$	$\rho\sigma^3 = 0.93743$	$\rho\sigma^3 = 1.03517$	$\rho\sigma^3 = 1.06$	$\rho\sigma^3 = 1.13$	$\rho\sigma^3 = 1.18$	$\rho\sigma^3 = 1.21$
500	-1.55(1)	-4.353(4)	-5.13(2)	-5.83(3)	-6.081(9)	-6.85(2)	-7.51(2)	-7.95(3)
2916	-1.546(5)	-4.349(1)	-4.893(9)	-5.86(3)	-6.104(9)	-6.88(2)	-7.53(2)	-7.98(3)
8788	-1.550(4)	-4.349(1)	-4.850(5)	-5.86(3)	-6.108(9)	-6.88(2)	-7.54(2)	-7.98(3)
∞	-1.548(4)	-4.3484(9)	-4.835(8)	-5.8613(9)	-6.1097(4)	-6.8844(5)	-7.5388(7)	-7.984(1)

B. Path 2: Tether length integration

Considering path 2 in Fig. 3, simulations at constant density with varying tether lengths are performed at the same densities but are extended to include one liquid density of $\rho\sigma^3 = 0.5$. In the liquid state, simulations are run from $r_T/\sigma \in [r_{T,0}/\sigma, 13]$ with a spacing of 0.02 for $r_T/\sigma \leq 4$ and 0.25 above $r_T/\sigma > 4$. In the solid phase, simulations are run from $r_T/\sigma \in [r_{T,0}/\sigma, 10]$ with a spacing of 0.01σ for $r_T/\sigma \leq 0.5$ and 0.1 above $r_T/\sigma > 0.5$. The individual entropy values are reported in Table II, including the linear extrapolation in N^{-1} to the thermodynamic limit. Extrapolations are again extremely linear, raising no concerns on the approach.

C. Comparison of approaches

The extrapolated results for both approaches are presented in Table III. To generate reference literature values, thermodynamic integration is performed on the current best available equations of state.²² The reference absolute crystal entropy of $s^{\text{res}}(\rho\sigma^3 = 1.04086)/k_B = -5.9189(2)$ is also taken from Ref. 22. Overall, the agreement between both the methods and against the literature is excellent, verifying the methods and the extrapolation to the thermodynamic limit. The calculated liquid entropy value is also in excellent agreement with other reported values [i.e., $-1.541(2)$ from Ref. 11]. Averaging over all results for path 2 using thermodynamic integration, our estimate for the reference crystal entropy is $s^{\text{res}}(\rho\sigma^3 = 1.04086)/k_B = -5.9168(4)$. This estimate for the crystal free energy can be used with the latest equations of state²² to estimate the fluid–solid coexistence point at a reduced liquid number density of $0.93890(7)$, a reduced solid density of $1.03715(9)$,

TABLE III. Residual entropy for the hard-sphere system for various number densities calculated using both approaches. The reference values are calculated using the equations of state and crystal entropy reported by Pierczyk *et al.*²² The uncertainty in the last reported digit is given in parenthesis.

$\rho\sigma^3$	s^{res}/k_B		
	Path 1	Path 2	Reference 22
0.5	...	-1.548(4)	-1.54670
0.9	...	-4.3484(9)	-4.37009
0.93743	...	-4.835(8)	-4.79695
1.03517	...	-5.8613(9)	-5.8633
1.06	-6.1078(4)	-6.1097(4)	-6.1106
1.13	-6.8835(3)	-6.8844(5)	-6.8846
1.18	-7.5377(4)	-7.5388(7)	-7.5388
1.21	-7.9906(4)	-7.984(1)	-7.9919

a reduced chemical potential of $16.053(4)$, and a reduced pressure of $11.550(4)$. The uncertainties on these values result from a propagation of uncertainty from the reference crystal energy above and not any uncertainty in the equations of state. Overall, these values are all in close agreement with the highly precise literature values, concluding that both approaches are reliable methods for extracting measurements of the entropy.

Both approaches outlined here are high-precision routes to the free energy with comparable computational costs; however, path 2 is more convenient as it can be applied to liquid and crystalline states. Path 1 also requires a careful selection of the tether length to avoid transitions; however, path 2 avoids this difficulty. The variation of tether and particle collisions with the tether length calculated with Path 2 may also provide further insight into the structure of phase space, which is completely inaccessible in normal simulation. This is briefly discussed in the conclusions, but further research is necessary to understand the full insight available.

V. CONCLUSIONS

In this work, the behavior of the tether particle model, first introduced by Speedy,⁴ is examined in detail. The variation of the compressibility factor with density is shown for tethered particle systems with different tether lengths. For the standard hard-sphere system and for the tethered system with sufficiently large tethers, there is a signature “kink” in the curve, signaling a first order transition between the liquid and solid phases. This “kink” is shown to weaken and vanish with the decreasing tether length. Therefore, for sufficiently short tether lengths, there is a continuous thermodynamic path between the fluid and solid states. At very low densities where spheres are spaced too far apart to interact, the tether system will reach an ideal state, which is analytically solvable; the free energy of this state is known exactly with respect to the “standard” ideal gas state. At sufficiently high densities, which occur in the solid phase, sphere–sphere collisions prevent the tether interactions, and the tether system becomes indistinguishable from the standard hard-sphere system. Therefore, thermodynamic integration can be directly used on MD simulations of the TPM for sufficiently short tether lengths to compute the free energy of solid hard-sphere systems. This method is shown to give highly precise estimates of the free energy in the solid state.

By considering the tethered hard-sphere system from the perspective of its motion through phase space, the rates of “collision” of the system with the bounding surfaces that encapsulate the phase space the system is allowed to explore are directly related to the area of the bounding surface. For boundaries that correspond to

sphere–sphere contacts, this relation can be used to derive the collision rate expression for the pressure. These surfaces can be shifted by increasing parameters, such as the sphere diameter or the tether length. Integrating the collision rates of the particles with the tether potentials, we can directly determine the entropy of the system with respect to the ideal TPM. This is found to be an efficient method for calculating the entropy of hard-sphere systems in any state.

The decay of the tether collision rate with the tether length was found to exhibit two types of behaviors depending on whether the system is fluid or solid. If the system is fluid, the cell collision rate approaches the cell collision rate of an ideal TPM as the tether becomes increasingly large [see Fig. 5(a)]. In the solid phase, the cell collision rate decays exponentially to zero as the tether is lengthened (see Fig. 5) and eventually vanishes. As the tether is lengthened, portions of the boundary in phase space corresponding to the tether interactions pass “behind” the boundary corresponding to sphere–sphere contacts, and it becomes increasingly more hidden from the system. As a result, the tether collision rate decreases. Eventually, tether collisions no longer occur, indicating that the tether boundary is completely hidden behind the sphere–sphere contact boundary and is no longer accessible by the system. In this situation, the sphere–sphere interactions confine the system to a relatively small region of phase space.

Interestingly, at lower densities that are near solid coexistence density, the decay of the tether collision rate no longer monotonically decreases with the tether length, dramatically increasing in value in some regions and even switching its qualitative decay to zero. As an example, in Fig. 8, the event rates for a system of particles tethered to an FCC lattice at $\rho\sigma^3 = 0.93743$ are shown. This is very near the fluid freezing density, and as the tether is lengthened, the cell collision rate decays rapidly toward zero, similar to that found for high density systems in the solid phase. The sphere–sphere collision rate appears to approach a limiting value, which corresponds to a solid-like pressure; for comparison, the collision rate in a solid at $\rho\sigma^3 = 0.93743$ is depicted as the dashed–dotted

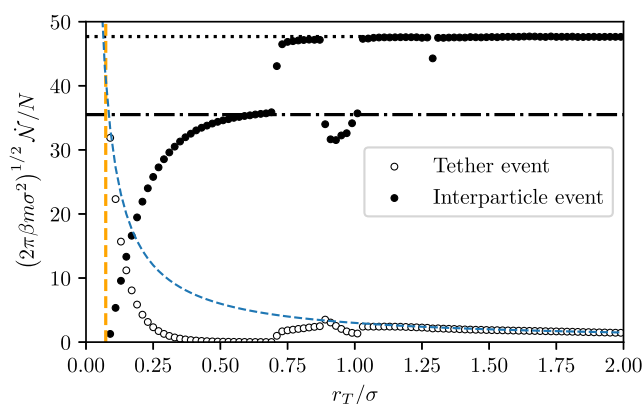


FIG. 8. Variation of the tether (unfilled circles) and inter-particle (filled circles) event rate as a function of the radius of the tether for an $N = 8788$ hard-sphere system tethered to an FCC lattice at $\rho\sigma^3 = 0.93743$. The dotted horizontal line is the particle–particle collision rate in the fluid phase, and the dashed–dotted horizontal line is the particle–particle collision rate in the FCC solid phase, as correlated by Pieprzyk *et al.*²² The dashed line is the tether event rate in the ideal fluid.

line in Fig. 8. At $r_T/\sigma \approx 0.69$, the tether collision rate “suddenly” begins to increase, and the sphere–sphere collision rate “jumps” to a much greater value, which corresponds to a liquid-like pressure; the sphere–sphere collision rate for a solid at $\rho\sigma^3 = 0.93743$ is depicted in Fig. 8. Truncating at $\rho\sigma^3 = 0.93743$ and integrating using Eq. (25) for solids give a residual entropy of $s^{res} = -4.96(2)$, which is remarkably close to the FCC value of $s^{res} = -4.9636(4)$ from extrapolating the equation of state (EOS). While both approaches are being used outside of their range of applicability, their agreement suggests that the tether model can be used to sample free energies of unstable configurations, provided that there is a clear opportunity where the tether rates approach either zero or the ideal limit. At longer tether lengths in Fig. 8, the tether event rate begins to approach the ideal TPM value after two “re-entries,” which is expected if the fluid is the stable phase. This behavior is reproducible and not due to the lack of equilibration of the simulations and is largely independent of system size for sufficiently large systems. It suggests that the FCC phase can still be distinguished from the fluid phase using this tether approach. The ability to separate unstable and stable configurations at the same density from each other with the tether length may help to provide further insight into phase transitions in other systems, such as two-dimensional hard disks, where this distinction is not clear and is a focus of our future work.

The relationship of the tether collision rates with the geometry of phase space allows the closer examination of the transition pathways between regions of phase space. The surface area of the phase space boundary corresponding to the tether contacts that are exposed to the system represents the cross-sections of the “hallways” through which the system can travel. The collision rate of the tether allows the determination of the surface area of sections of phase space not blocked off by sphere overlaps. By increasing the tether length, we can observe how the area of this transition hallway varies. This allows the identification of bottlenecks, where this area reaches a minimum, between regions of phase space that correspond to different “macrostates” of the system (e.g., fluid and crystalline). The tether collision rate depicted in Fig. 8 corresponds to a system where the FCC crystal region of phase space is connected to the fluid region through relatively narrow pathways. The “areas” of these paths can be quantified, which with further analysis can be used to estimate transition rates between these states. We are currently exploring developing this approach to examine the transition states and pathways of different systems, such as the nucleation of crystals in hard-sphere systems and the folding of polymers in helix forming systems.^{23–25}

While the scope of this paper has been limited to single component systems, the expressions in this work can easily be extended to any multicomponent, discontinuous potential system. Additionally, in this work, the tethering potential was considered to act on single spheres, confining them to be located within a cell; however, this is only one example of a tethering potential. Many other alternatives are possible, and they can be considered in much more general terms. For example, the tethering potential might act between pairs of spheres in order to keep them within a set distance from one another. This type of tethering simulation can be used to obtain the potential of mean force between particles or collections of particles, such as polymer chains. Another example is to confine a group of spheres to within a certain cell. This would allow the calculation of the entropy penalty of clustering spheres

to form aggregates. These offer interesting directions for future work.

ACKNOWLEDGMENTS

The authors acknowledge the support of the Maxwell computing service at the University of Aberdeen and the Aberdeen-Curtin Alliance²⁶ between the University of Aberdeen (Scotland, UK) and Curtin University (Perth, Australia), which funded the Ph.D. of C.M.

DATA AVAILABILITY

The data that support the findings of this study are available from the corresponding author upon reasonable request.

REFERENCES

- W. G. Hoover and F. H. Ree, "Melting transition and communal entropy for hard spheres," *J. Chem. Phys.* **49**, 3609 (1968).
- L. V. Woodcock, "Computation of the free energy for alternative crystal structures of hard spheres," *Faraday Discuss.* **106**, 325–338 (1997).
- L. V. Woodcock, "Entropy difference between the face-centred cubic and hexagonal close-packed crystal structures," *Nature* **385**, 141–143 (1997).
- R. J. Speedy, "The entropy of a glass," *Mol. Phys.* **80**, 1105–1120 (1993).
- A. Donev, F. H. Stillinger, and S. Torquato, "Calculating the free energy of nearly jammed hard-particle packings using molecular dynamics," *J. Comput. Phys.* **225**, 509–527 (2007).
- D. Frenkel and A. J. C. Ladd, "New Monte Carlo method to compute the free energy of arbitrary solids. Application to the fcc and hcp phases of hard spheres," *J. Chem. Phys.* **81**, 3188–3193 (1984).
- D. Frenkel and B. Smit, *Understanding Molecular Simulation: From Algorithms to Applications*, 2nd ed. (Academic Press, San Diego, CA, 2002).
- M. B. Sweatman, "Self-referential Monte Carlo method for calculating the free energy of crystalline solids," *Phys. Rev. E* **72**, 016711 (2005).
- M. B. Sweatman, A. A. Atamas, and J.-M. Leyssale, "The self-referential method combined with thermodynamic integration," *J. Chem. Phys.* **128**, 064102 (2008).
- M. B. Sweatman, A. Atamas, and J.-M. Leyssale, "The self-referential method for linear rigid bodies: Application to hard and Lennard-Jones dumbbells," *J. Chem. Phys.* **130**, 024101 (2009).
- T. Schilling and F. Schmid, "Computing absolute free energies of disordered structures by molecular simulation," *J. Chem. Phys.* **131**, 231102 (2009).
- U. R. Pedersen, "Direct calculation of the solid-liquid Gibbs free energy difference in a single equilibrium simulation," *J. Chem. Phys.* **139**, 104102 (2013).
- M. B. Sweatman, "Comparison of absolute free energy calculation methods for fluids and solids," *Mol. Phys.* **113**, 1206–1216 (2015).
- W. G. Hoover, C. G. Hoover, and M. N. Bannerman, "Single-speed molecular dynamics of hard parallel squares and cubes," *J. Stat. Phys.* **136**, 715 (2009).
- E. P. Bernard, W. Krauth, and D. B. Wilson, "Event-chain Monte Carlo algorithms for hard-sphere systems," *Phys. Rev. E* **80**, 056704 (2009).
- J. D. Weeks, D. Chandler, and H. C. Andersen, "Role of repulsive forces in determining the equilibrium structure of simple liquids," *J. Chem. Phys.* **54**, 5237–5247 (1971).
- M. N. Bannerman, R. Sargant, and L. Lue, "DynamO: A free $\mathcal{O}(N)$ general event-driven molecular dynamics simulator," *J. Comput. Chem.* **32**, 3329–3338 (2011).
- R. J. Speedy, "Statistical geometry of hard-sphere systems," *J. Chem. Soc., Faraday Trans. 2* **76**, 693–703 (1980).
- W. G. Hoover, W. T. Ashurst, and R. Grover, "Exact dynamical basis for a fluctuating cell model," *J. Chem. Phys.* **57**, 1259–1262 (1972).
- L. Lue, "Collision statistics, thermodynamics, and transport coefficients of hard hyperspheres in three, four, and five dimensions," *J. Chem. Phys.* **122**, 044513 (2005).
- M. N. Bannerman and L. Lue, "Exact on-event expressions for discrete potential systems," *J. Chem. Phys.* **133**, 124506 (2010).
- S. Pieprzyk, M. N. Bannerman, A. C. Brańka, M. Chudak, and D. M. Heyes, "Thermospheres and dynamical properties of the hard sphere system revisited by molecular dynamics simulation," *Phys. Chem. Chem. Phys.* **21**, 6886–6899 (2019).
- J. E. Magee, V. R. Vasquez, and L. Lue, "Helical structures from an isotropic homopolymer model," *Phys. Rev. Lett.* **96**, 207802 (2006).
- J. E. Magee, L. Lue, and R. A. Curtis, "Density of states for a short overlapping-bead polymer: Clues to a mechanism for helix formation?," *Phys. Rev. E* **78**, 031803 (2008).
- M. N. Bannerman, J. E. Magee, and L. Lue, "Structure and stability of helices in square-well homopolymers," *Phys. Rev. E* **80**, 021801 (2009).
- See <http://aberdeencurtinalliance.org> for information on the international collaboration between the University of Aberdeen and Curtin University.